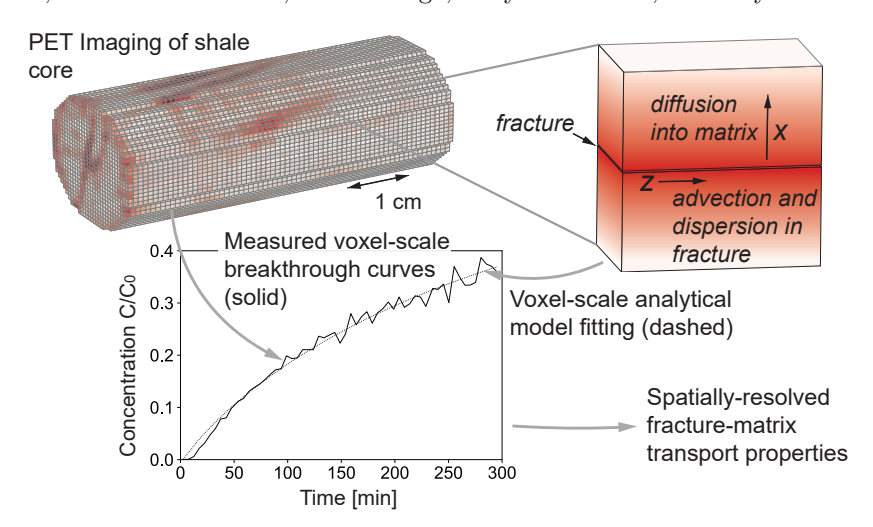
# Graphical Abstract

- Quantification of the impact of acidified brine on fracture-matrix
- 3 transport in a naturally fractured shale using in situ imaging and
- 4 modeling
- 5 Christopher Zahasky, Manju Pharkavi Murugesu, Takeshi Kurotori, Collin Sut-
- 6 ton, Jennifer L. Druhan, Bolivia Vega, Sally M. Benson, Anthony R. Kovscek



Quantification of the impact of acidified brine on fracture-matrix transport in a naturally fractured shale using in situ imaging and modeling

Christopher Zahasky<sup>a,\*</sup>, Manju Pharkavi Murugesu<sup>b</sup>, Takeshi Kurotori<sup>b</sup>, Collin Sutton<sup>a</sup>, Jennifer L. Druhan<sup>c</sup>, Bolivia Vega<sup>b</sup>, Sally M. Benson<sup>b</sup>, Anthony R. Kovscek<sup>b</sup>

#### 3 Abstract

10

11

Understanding flow, transport, chemical reactions, and hydro-mechanical processes in fractured geologic materials is key for optimizing a range of subsurface processes including carbon dioxide and hydrogen storage, unconventional energy resource extraction, and geothermal energy recovery. Flow and transport processes in naturally fractured shale rocks have been challenging to characterize due to experimental complexity and the multiscale nature of quantifying continuum scale descriptions of mass exchange between micrometer-scale fractures and nanometer-scale pores. In this study, we use positron emission tomography (PET) to image the transport of a conservative tracer in a naturally fractured Wolfcamp shale core before and after exposure of the core to low pH brine conditions. Image-based experimental observations are interpreted by fitting an analytical transport model to fracture-containing voxels in the core. Results of this analysis indicate subtle increases in matrix diffusivity and a slightly more uniform fracture velocity distribution following exposure to low pH conditions. These observations are compared with a multi-component one-dimensional reactive transport model that indicates the capacity for a 10% increase in porosity at the fracture-matrix interface as a result of the low pH brine exposure. This

<sup>&</sup>lt;sup>a</sup> Department of Geoscience University of Wisconsin-Madison Madison WI 53706 United States

<sup>&</sup>lt;sup>b</sup>Department of Energy Science & Engineering Stanford University Stanford CA 94305 United States

<sup>&</sup>lt;sup>c</sup>Department of Geology University of Illinois at Urbana-Champaign Urbana IL 61801 United States

<sup>\*</sup>Corresponding author email: czahasky@wisc.edu

porosity change is the result of the dissolution of carbonate minerals in the shale matrix to low pH conditions. This image-based workflow represents a new approach for quantifying spatially-resolved fracture-matrix transport processes and provides a foundation for future work to better understand the role of coupled transport, reaction, and mechanical processes in naturally fractured rocks.

14 Keywords: shale, fractures, X-ray computed tomography, positron emission

tomography, reactive transport, models

#### 1. Introduction

A quantitative and predictive understanding of transport across fracturematrix interfaces in shale formations is vital to the management and engineering
of a range of flow and transport processes. These processes include groundwater
protection from infiltrating contaminants [1], storage security of geologically
sequestered CO<sub>2</sub> [2, 3, 4], resource recovery following hydraulic fracturing [5, 6,
7], and long-term nuclear waste storage security [8, 9].

Flow and transport processes between fractures and matrix/host rock material have been quantitatively described with a range of numerical and analytical

Flow and transport processes between fractures and matrix/host rock material have been quantitatively described with a range of numerical and analytical modeling approaches. Large fracture networks have been modeled with multiple interacting continua approaches (e.g. dual porosity, dual permeability) [10, 11, 12, 13, 14], or large discrete fracture networks where the fractures are explicitly defined [15, 16]. Simulation of flow in a small number of fractures can be accomplished using explicit flow field modeling by solving the Navier-Stokes equation when fracture geometry can be constrained or approximated [17, 18], or using hybrid or micro-continuum approaches [19, 20].

In addition to numerical approaches, analytical models have been derived to
describe solute and reactive transport in fractured systems [21, 22]. Describing
solute transport into matrix material with analytical models often relies on the
assumption that the matrix can be considered infinite and the concentration
of solute in the fracture is constant [21, 23]. A more sophisticated solution

was derived to account for advection and dispersion in the fracture [24]. Semianalytical solutions have been expanded to solve for these processes in two dimensions along a single fracture [25]. The advantage of these analytical methods is that they can be readily applied to solve for transport parameters within simple systems or sub-domains (i.e. voxels) within more complex systems.

A key barrier to predictive understanding of transport between fracture and 42 matrix in many geologic settings is quantifying flow and transport processes in response to changing fluid chemistry conditions. In many contexts, the overprinting of natural environmental conditions by anthropogenic activities results in transient variations in pore fluid chemistry that can drive precipitation and dissolution reactions that alter fracture-matrix transport behavior 47 [26, 27, 28, 20]. The mineralogical composition of shale rocks is often categorized into the proportion of shale matrix composed of carbonate minerals (e.g. calcite and dolomite), silicates (e.g. quartz, feldspars, and pyrite), and clays 50 (e.g. illite and smectite) [6] and these differences in composition have been 51 observed to influence local matrix transport properties [29]. In the presence of 52 complex brines, and when subject to rapid shifts in pH and solute chemistry, this multi-component and multispecies system presents a highly coupled, non-linear reactive transport problem [30] requiring numerical reactive transport models 55 to track and predict behavior [31, 32, 33, 34, 35, 30, 36, 37].

Multiscale quantification of flow, transport, and reactions is often complicated by uncertainty about the applicability of experimental batch measurements under ambient conditions to larger-scale dynamic system behavior [38]. In cases where flow-through experiments are performed under elevated pressure and temperature, typically only bulk measurements of transport properties are possible [39]. X-ray computed tomography (X-ray CT) is a key tool that has been extensively used to recover three-dimensional information about fracture geometry and fracture evolution under in situ conditions in geologic materials [40, 41, 42, 43, 44, 27, 4]. However, while X-ray CT is ideal for geometric quantification, measurement of solute transport is challenging with X-ray CT due to the need to use high photon attenuating tracers [45]. These tracers can create

gravitational artifacts and have very low signal-to-noise ratios as solute concentration decreases. These challenges are amplified in samples with micron-scale fracture apertures [46, 45, 47, 48].

Positron emission tomography (PET) is a complementary in situ imaging 71 technique that relies on the detection of high-energy photons produced from in-72 jected positron-emitting radiotracers. Tomographic reconstruction methods are 73 then used to acquire three-dimensional time-lapse images of radiolabeled compound distributions in geologic materials. This three-dimensional imaging provides thousands of concentration measurements as a function of time throughout 76 a sample, enabling multiscale transport quantification. The 511 keV photons 77 emitted during positron emission and annihilation events are ideally suited for 78 geologic materials that otherwise cause significant photoelectric adsorption and attenuation of lower energy photons [45]. This technique has recently been used to quantify solute advection and dispersion in highly heterogeneous sandstones 81 under saturated and unsaturated flow [49, 50, 51] and to quantify absorption in 82 microporous carbonates [52]. 83

In this study, we employ PET imaging to provide the unprecedented quantification of spatially variable fracture-matrix transport associated with natural fractures in a Wolfcamp formation shale sample before and after acidic reactive 86 fluid injection. Slug radiotracer injection with simultaneous PET imaging is per-87 formed and an analytical solution to the advection-dispersion equation is used to 88 interpret voxel-scale fracture-matrix transport. A weak acidified brine injection (pH=4) was then performed for 21 days followed by a repeated slug tracer imaging experiment. This second post-acid experiment enabled the quantification of 91 changes in transport behavior resulting from extended exposure to low pH con-92 ditions. A multi-component numerical reactive transport model (RTM) is con-93 structed to confirm the extent of reactive alteration based on acid-neutralizing solubilization of carbonate minerals at the fracture-matrix interface. The RTM offers independent verification of the interpretation of experimentally-observed 96 changes in fracture-matrix transport behavior.

## 8 2. Methods

## 2.1. Sample characterization and brine fluid chemistry

The core used in this study is a cylindrical Wolfcamp shale core with a 100 diameter of 25 mm and a length of 58 mm acquired from the Permian Basin at 101 a depth of 2867 m. Mineral composition and organic content of the core were 102 measured using X-ray diffraction analysis and source rock analysis, respectively. 103 Both measurements were conducted by Core Laboratories. Core mineralogy and 104 organic characteristics are shown in Table A.3 and were reported in previous 105 studies [53]. Synthetic brine was created following the Wolfcamp brine recipe 106 (Table 1) that was previously developed to establish chemical equilibrium with Wolfcamp shale, thus minimizing reactivity prior to the acidification experiment [37].109

Table 1: Composition of synthetic brine solution.

Composition	Potassium Chloride	Calcium Chloride	Magnesium Chloride	Sodium Chloride	Sodium Nitrate	Sodium Sulphate	Sodium Bicarbon-
wt%	1.1	5.23	1.49	90.9	0.06	0.80	0.39

## 2.2. Experimental CT data acquisition

The Wolfcamp core sample was first dried for 120 hours in a vacuum oven 111 at 45°C until the sample mass stabilized. The core was sealed between the 112 coreholder inlet and outlet end caps using high-strength heat-shrink fluorinated 113 ethylene propylene tubing. The core was then wrapped with an aluminum foil 114 to provide a gas diffusion barrier [54, 50]. The coreholder inlet and outlet end 115 caps had flow channels connecting to the core with dead volumes of 0.58 cm<sup>3</sup> 116 and 0.98 cm<sup>3</sup>, respectively. The core was placed into a high-pressure aluminum sleeve that enabled the application of confining pressure using tap water as the 118 confining fluid. The seal around the core was pressure-tested for 24 hours to 119 ensure complete isolation of pore fluids from the confining fluid.

Prior to pore fluid injection, a confining pressure of 1720 kPa (250 psi) was 121 applied and the sample was vacuumed using a vacuum pump (Leybold D16B, 122 ultimate pressure:  $1 \times 10^{-4}$  mbar). With the vacuum applied, the sample was 123 imaged daily using an X-ray CT scanner (GE LightSpeed) operated at 140 kV 124 and 120 mA with an exposure of 1 second per scan. The raw voxel size was 125  $195 \times 195 \times 625 \, \mu \text{m}^3$  and the field of view of was 10 cm. Complete vacuum was 126 reached when the CT number in Hounsfield units of the core ceased to decrease 127 further. These X-ray CT scans provide dry baseline scans for subsequent porosity and fluid saturation measurements and monitoring [41]. 129

The core was then saturated with krypton gas (99.999% purity) at 2068 kPa (300 psi) and confining pressure of 3790 kPa (550 psi). Krypton is an inert gas with a large X-ray attenuation coefficient relative to other gases [55]. The higher X-ray attenuation coefficient increases the contrast between the baseline scan and the krypton-saturated scan. This provides a more accurate quantification of the 3D porosity distribution in the core, which is calculated via linear scaling [41, 53].

The core was then vacuumed again and saturated with CO<sub>2</sub> (100% purity) 137 at 2068 kPa (300 psi) before injecting the prepared synthetic brine solution 138 described in Table 1. The core is saturated with CO<sub>2</sub> prior to brine injection 139 because of the higher solubility of CO<sub>2</sub> relative to air. This ensures that any 140 gas that is not displaced during brine injection will be dissolved in the brine 141 and transported out of the core [53]. To initially saturate the core, the brine was injected at a pressure of 3650 kPa (530 psi) with a backpressure of 3170 143 kPa (460 psi) and confining pressure of 4826 kPa (700 psi). Pyrite oxidation 144 was minimized by purging nitrogen gas through the injected brine used in all 145 experiments to displace any dissolved oxygen. All pressure conditions were 146 controlled by high-pressure syringe pumps (Teledyne ISCO) as schematically illustrated in Figure 1. The brine imbibition process was monitored and the core was determined to be fully saturated based on X-ray CT scans [53]. 149

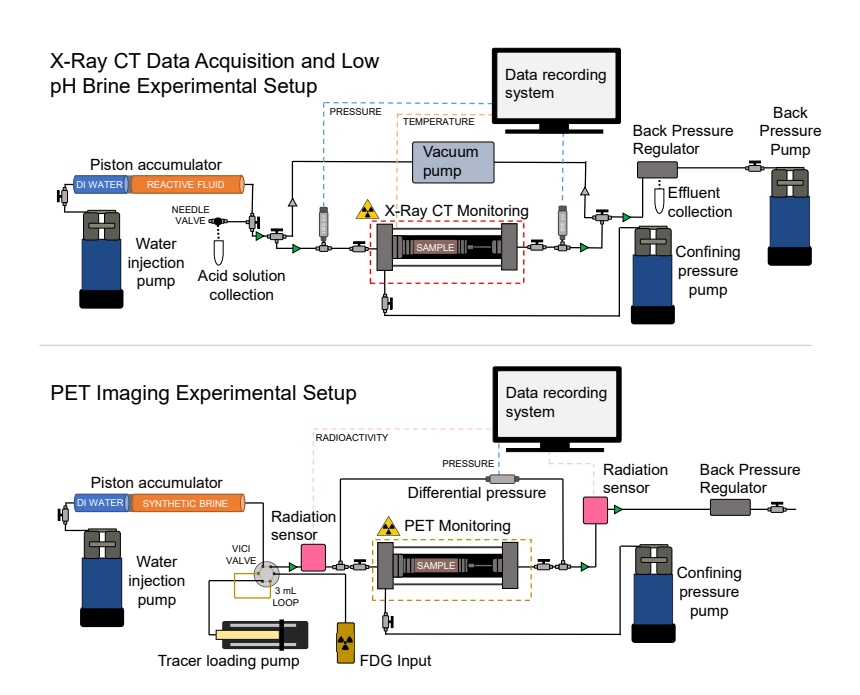


Figure 1: Schematic illustrations of the experimental setups for reaction (top) and PET imaging experiments (bottom).

## 2.3. Experimental positron emission tomography data acquisition

150

178

179

Two sets of tracer experiments imaged with PET were performed, one before 151 the low-pH brine injection and one after the low-pH brine injection as described in the following section. PET imaging experiments were performed with an ex-153 perimental platform schematically described in the lower illustration of Figure 154 1. This platform is specifically designed for the safe injection, quantification, 155 and disposal of radiotracers with simultaneous in situ PET imaging. Continu-156 ous aqueous phase injection was achieved with a Vindum VP-3K dual piston 157 pump plumbed to a 1000 mL Parker piston accumulator filled with the brine 158 mixture described in Table 1. The fluid injection rate for both PET imaging 159 experiments was 0.01 mL/min. The pore pressure conditions at this flow rate 160 were approximately 2000 kPa (290 psi), with the post-reaction pore pressure 161 being slightly higher due to the reduction of sample permeability resulting from low pH brine exposure. A second Vindum VP-6K dual piston pump applied a 163 confining pressure to the core of 3790 kPa (550 psi). This confining pressure 164 was used in all PET imaging and low-pH brine injection procedures. 165

The positron-emitting radiotracer [18F]-fluorodeoxyglucose (FDG) was used 166 for the imaging experiments. This commercially available radiotracer has a 167 half-life of 109.7 minutes and has been found to behave as an ideal tracer in 168 a range of geologic materials in part because of the charge neutrality of FDG. 169 Fluorodeoxyglucose was diluted in 3 mL of the brine described in Table 1 to 170 reach the optimal radioactivity concentration for minimizing imaging noise [45]. Precise control of the radiotracer injection and timing was controlled using a 172 six-port dual-position VICI Cheminert HPLC rotary valve with a 3 mL in-173 jection loop. Pressure and radiation sensors enabled continuous measurement 174 of fluid pressure, pump pressures, and injected radiotracer concentration. To 175 safely handle radioactive liquids, the experimental system utilized extensive lead 176 shielding around the radiation sources.

The PET scans were performed using a *Siemens Inveon DPET* pre-clinical scanner at the University of Wisconsin-Madison small animal imaging and radiotherapy facility (SAIRF). Each experiment was completed in 12 hours with four

three-hour scans. Due to the length of the experiment, the image timesteps were discretized into 5-minute intervals. However, PET imaging enables timesteps as short as 20 seconds to monitor more rapid transport processes [45]. Sequential PET scans were concatenated together in time by decay correcting to the scan start time [48]. Confirmation of tracer mass balance after image concatenation is illustrated in Figure B.9 in Appendix B. Additional details and theoretical background related to PET imaging experiments in geologic materials are described in previous work [45].

#### 2.4. Low-pH brine injection experimental procedure

205

207

208

209

Following the first PET scan, the core was exposed to continuous flow-190 through of pH 4.0 brine analogous to conditions that might occur when brine is saturated with dissolved CO<sub>2</sub>. To perform this experiment, the core was 192 again connected to a pump containing the synthetic brine mixture described in 193 Table 1. The experimental setup is illustrated in the upper pane of Figure 1. 194 Brine was injected through the core for a period of seven days (approximately 195 100 mL) to ensure the displacement of any remaining FDG in the core. The 196 injection line of the core was then connected to a piston accumulator (Parker 197 A3NW0058D1E with a nickel coating) containing the brine solution with the 198 addition of hydrochloric acid (Baker Analyzed, assay: 37.1%, density: 2.7 kg/1 199 L). This produced a brine solution with a pH of 4.0 that was then injected 200 continuously at a constant pressure of 2200 kPa (320 psi), backpressure of 1510 kPa (220 psi), and confining pressure of 3790 kPa (550 psi) for 21 days. The 202 reacted brine was produced at the outlet. At these conditions, a total of 55.4 203 pore volumes of weakly acidic brine was injected over a period of 21 days. 204

Throughout the pH 4.0 brine injection, the core sleeve was covered with heat tape and insulated to maintain a constant temperature of 40 °C. This temperature regulation was principally employed to more closely represent in situ reservoir conditions. Following the 21 day injection, a second conservative tracer PET scan was performed under identical conditions as the first PET experiment as described in Section 2.3.

## 2.5. Fracture identification and PET image processing

To quantify fracture-matrix transport, the raw PET scans were segmented 212 into voxels containing fractures and voxels not containing fractures. The raw 213 data was first coarsened by a factor of three, giving a voxel size of 2.3 mm  $\times$  2.3 mm × 2.3 mm. Raw images were coarsened by a factor of three by taking the 215 arithmetic average of  $3\times3\times3$  voxels, thereby also reducing the number of voxels 216 by a factor of 27. Coarsening was performed to reduce imaging noise [45] and to 217 ensure that the voxels were large enough to capture the majority of the solute that diffused into the matrix over the duration of the experiment. This voxel size 219 also results in a fracture-to-matrix volume that enables the quantity of the tracer 220 in the fracture to be neglected from analytical model fitting. The radiotracer 221 in the fracture is assumed to be negligible because the fracture apertures were 222 estimated to be in the tens of micrometers or less based on the X-ray CT 223 images and therefore occupied less than one percent of the coarsened voxel volume. Coarsened voxels containing fractures were identified by first applying 225 the Frangi vesselness filter [56]. The Frangi filter has been used to detect image 226 features such as vessels, wrinkles, and rivers [57, 58]. Filtered images were then 227 thresholded to select voxels in the core that most likely correspond to voxels containing fractures. 229

## 230 2.6. Semi-analytical fracture matrix transport model description

Once voxels containing fractures were identified from the PET images, an 231 analytical transport model was fit to each voxel breakthrough curve. An analyt-232 ical solution was employed that accounts for advection and dispersion along the 233 fracture and diffusion into the matrix [24]. Solute dispersion within the fracture 234 results from mechanisms that drive spatial variability in fluid velocities such 235 as Taylor dispersion, fracture roughness, and aperture variability [59, 60, 61]. 236 Fitting the analytical solution to each voxel breakthrough curve enabled the voxel-scale estimation of matrix tortuosity  $(\tau')$ , local fracture longitudinal dis-238 persivity  $(\alpha_z)$ , and local fracture advection velocity  $(v_z)$ .

The differential equation for solute transport in the fracture is given by

$$\frac{\partial C}{\partial t} - D_z \frac{\partial^2 C}{\partial z^2} + v_z \frac{\partial C}{\partial z} + \frac{q}{b} = 0 \tag{1}$$

Here,  $D_z$  is the hydrodynamic dispersion coefficient in the fracture that can be defined by  $D_z = \alpha_z v_z + \mathcal{D}$  where  $\mathcal{D}$  is the bulk molecular diffusion coefficient in water. A value of molecular diffusion of  $\mathcal{D} = 6.7\text{e-}6$  [cm<sup>2</sup>/s] was assumed based on the diffusion coefficient of glucose in water. The variable q is the diffusive flux perpendicular to the fracture face and b is half of the fracture aperture. The mean fracture aperture was roughly estimated to be 20  $\mu$ m using the calibration-free missing attenuation method [48] on the X-ray CT scan shown in Figure 2.

Advection into the matrix is assumed to be negligible so that solute transport can be described by the diffusion equation.

$$\frac{\partial C'}{\partial t} - D' \frac{\partial^2 C'}{\partial x^2} = 0 \tag{2}$$

The notation C' explicitly denotes the concentration of solute in solution in the matrix following the original notation of Tang et al [24]. The variable D'248 is the effective diffusion coefficient in the matrix that is related to the bulk 249 liquid diffusion coefficient ( $\mathcal{D}$ ) by  $D' = \tau' \mathcal{D}$ , where  $\tau'$  is the matrix tortuosity 250 [62, 24] or sometimes referred to as the diffusibility [63]. Note that this is 251 related to another common definition of tortuosity  $(\tau)$  often found in literature, sometimes also termed the lithologic factor [62] or matrix factor [63]. This  $\tau$ 253 term refers to the distance some particle must travel through a porous media 254 relative to the straight line distance. These two definitions are related by the 255 expression  $\tau' = \phi/\tau$ , where  $\phi$  is the matrix porosity [62, 64, 65]. However other 256 relationships with porosity have been proposed in literature [63]. For clarity,  $\tau'$ will be referred to as the matrix tortuosity throughout this manuscript.

The concentration gradient  $(\partial C'/\partial x)$  at the fracture-matrix interface is related to the diffusive flux (q) in Equation 1 by the following equation.

$$q = -\theta D' \frac{\partial C'}{\partial x} \bigg|_{x=b} \tag{3}$$

Equation 3 can then be substituted into Equation 1 to obtain the coupled equation for advection and dispersion in the fracture and orthogonal diffusion into the matrix.

$$\frac{\partial C}{\partial t} - D_z \frac{\partial^2 C}{\partial z^2} + v_z \frac{\partial C}{\partial z} - \frac{\theta D'}{b} \frac{\partial C'}{\partial x} \bigg|_{x=b} = 0 \tag{4}$$

The solution for matrix concentration (C') at a distance (z) from the inlet of the core, a distance (x) from the center of the fracture as a function time t has been previously derived [24]. Specifically, for the following boundary and initial conditions

$$C(0,t) = C_0 \tag{5}$$

$$C(\infty, t) = 0 \tag{6}$$

$$C(z,0) = 0 (7)$$

$$C'(b, z, t) = C(z, t) \tag{8}$$

$$C'(\infty, z, t) = 0 \tag{9}$$

$$C'(x, z, 0) = 0 (10)$$

the solution for matrix concentration (C') based on the coupled equation is given by Equation 11. Note that  $C_0$  is the source concentration.

$$\frac{C'}{C_0} = \frac{\exp(\nu z)}{\pi^{1/2}} \int_l^{\infty} 2 \exp\left[-\xi^2 - \frac{\nu^2 z^2}{4\xi^2}\right] \exp(-\eta z^2) \operatorname{erfc}\left[\frac{Y'}{2T}\right] d\xi \qquad (11)$$

Here T and Y' are given by Equation 12 and 13, respectively.

$$T = \sqrt{t - \frac{z^2}{4D_z \xi^2}} \tag{12}$$

$$Y' = \frac{v^2 \beta^2 z^2}{4A\xi^2} + B(x - b) \tag{13}$$

Variables  $\nu$  and  $\beta$  are defined as  $\nu = v/2D_z$  and  $\beta = \sqrt{4D_z/v^2}$ . The lower limit of the integral (l) in Equation 11 is equal to Equation 14.

$$l = \frac{z}{\sqrt{4D_z t}} \tag{14}$$

Additional mathematical derivation details can be found in Tang et al. [24].

Note that unlike the original solution in [24], the first-order reaction/decay terms

are neglected because all of the reconstructed PET data are decay corrected

based on the 109.7 min half-life of <sup>18</sup>F.

Equation 11 was solved with a two-step composite trapezoidal function pro-265 grammed in Python. The first step was to determine the upper limit of the 266 integral in Equation 11—below which the integrand is greater than zero. The 267 second step was to then solve the integral between l and this upper limit with a very fine discretization of  $\xi$ . This two-step numerical method was found to 269 be more numerically efficient than the Gaussian quadrature method. To fit 270 this equation to the volume-average concentrations in each fracture-containing 271 voxel as a function of time, Equation 2 was solved as a function of distance into 272 the matrix (x) at each time step. This resulted in a concentration profile as a function of distance x from the fracture center to the voxel edge—assuming 274 the fracture was in the middle of the voxel. This profile was then integrated as 275 a function of x from each side of the fracture and divided by the voxel width 276 to calculate the expected average voxel concentration of radiotracer at a given 277 time. To fit the analytical model to the measured breakthrough data, a non-278 linear least squares fitting routine was developed using SciPy package functions. 279 The processed data and Python codes used for analysis and analytical modeling 280 are available in the data repository cited in the Acknowledgements. 281

#### 282 2.7. One-dimensional reactive transport simulation

A multi-component RTM was developed to quantify the extent of fracturematrix alteration during low pH fluid injection and independently verify the
extent of alteration suggested by the experimental results and fracture-matrix
transport model. A one-dimensional (1D) RTM was constructed in the opensource numerical reactive transport software CrunchFlow [35]. The RTM tracks
changes in mineral volumes resulting from solubilization due to exposure to the
through-flowing weakly acidic brine. The initial mineral volumes used for the
RTM are given in Table 2. The mineral volumes were determined based on min-

eral densities and the weight percents measured in the core and reported in Table
A.3, and rounded to the nearest integer. The starting mineralogy includes plagioclase, specifically albite, and clays including smectite and illite. The injected
fluid chemistry composition is based on the laboratory brine described in Table
1. Mineral reaction kinetics, temperature-dependent equilibrium coefficients,
and multi-component aqueous speciation including the carbonate equilibria and
associated feedbacks to pH, as shown in Table C.4 and C.5, are all included in
the model based on prior Wolfcamp RTM simulations [5, 6, 7].

The model domain was oriented to allow transport perpendicular to the 299 plane of the fracture with one end of the model representing the fracture-matrix 300 interface and the other end representing the no-flow walls of the core. The 301 length of the model was 12.6 millimeters long and 1 millimeter wide. The 302 bulk diffusion of HCl in water is  $\mathcal{D} = 5.25 \text{e-} 5 \text{ cm}^2/\text{sec}$  [66]. To set the model diffusion, the bulk diffusion was multiplied by  $\tau' = 0.0125$ . The pressure drop 304 from the fracture into the matrix was assumed to be low and was set to 6.9 kPa 305 (1 psi). The temperature was set to 40 °C. The permeability of the matrix was 306 approximated as 10  $\mu$ D as estimated based on steady-state differential pressure 307 following core saturation with brine. The starting porosity of the model was 308 10.2 percent as measured with the X-ray CT scan and identical to the value 300 used for the analytical transport model. The model input files and database are 310 available in the data repository cited in the Acknowledgements. 311

Table 2: Starting mineral volume fractions of the Wolfcamp sample specified in the reactive transport simulation.

Mineral	Quartz	K-Feldspar	Albite	Calcite	Dolomite	Pyrite	Illite	Smectite	
vol%	57	1	4	0	3	1	22	1	Ī

#### 2 3. Results

3.1. Fracture identification and concentration quantification with PET imaging 313 The core and fracture geometry is illustrated in the X-ray CT scan in Figure 314 2. The CT scan depicts one nearly through-going bedding-parallel fracture that 315 intersects the inlet face of the core. There are several other small microfractures 316 semi-parallel to this main fracture, including several that intersect the outlet 317 face of the core. The results of the radiotracer injection and imaging with PET 318 prior to acid exposure are illustrated in Figure 3. The red shading indicates 319 radiotracer concentration in uncoarsened PET images in different slices along 320 the axis of the core. The PET images clearly show the transport of radiotracer 321 through these fractures identified in the X-ray CT scan. 322

Radiotracer injection and imaging before and after acid exposure are shown 323 in Figures 3 and 4, respectively. Results of the coarsened and thresholded voxels 324 containing fractures are highlighted by the grey shading in Figure 3 (pre-acid in-325 jection) and Figure 4 (post-acid injection). The threshold was selected such that 326 there was a very high degree of confidence that the voxel contained the fracture and was not influenced by core boundary conditions. As a result, many vox-328 els that likely contained fractures were neglected from the analytical parameter 329 fitting. Regardless of these neglected voxels, there were 156 voxels thresholded 330 in the pre-acid scan and 153 voxels thresholded in the post-acid scan. Note that while many of these voxels were in identical locations as can be seen by 332 comparing Figures 3 and 4, the thresholding workflow did not include a routine 333 to select identical sets of fracture-containing voxels due to subtle differences in 334 image registration between the scans. 335

#### 3.2. Voxel-scale transport quantification

336

Figures 5 and 6 show the results of fitting the analytical model (right plots)
to the fracture-containing voxel breakthrough curves (left plots) before and after low-pH brine injection, respectively. The initial breakthrough of tracer in
different voxels varied as a function of position along the length of the fracture.

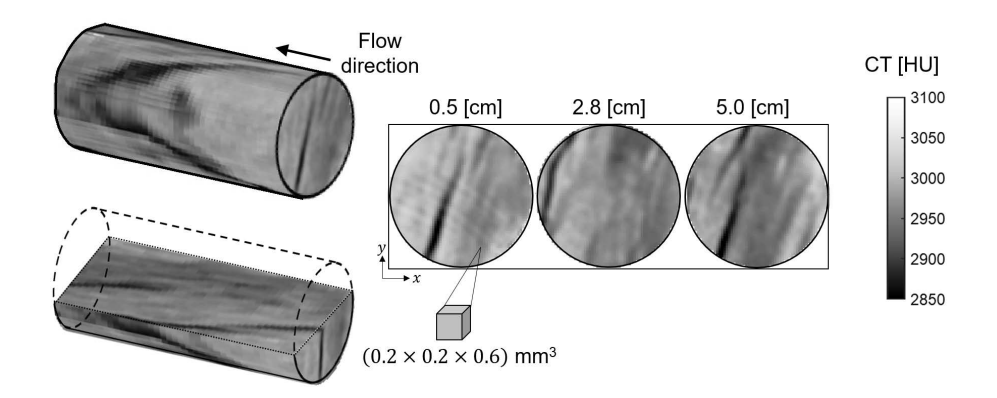


Figure 2: X-ray CT image of the Wolfcamp shale core. The two-dimensional slices illustrated on the right highlight the geometry of the fracture (darker regions) prior to low-pH fluid injection. The slices are taken at increasing distances from the inlet (z=0). The grey colorscale in all images is in Hounsfield units [HU].

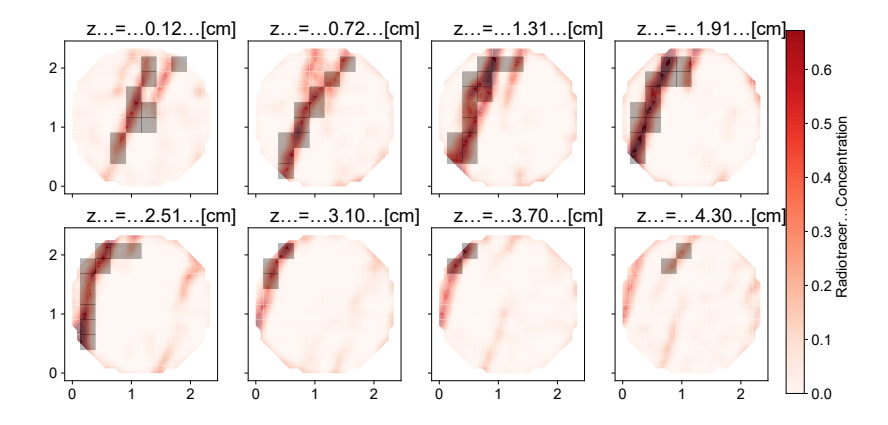


Figure 3: Two-dimensional slices through the core in the PET scan prior to acid exposure after 144 minutes of tracer injection. The slices are at increasing distances from the inlet (z=0). X and Y axes are length scales in centimeters. The red color scale illustrates the radiotracer concentration and the shaded grey boxes highlight the thresholded voxels used for fitting the analytical transport model.

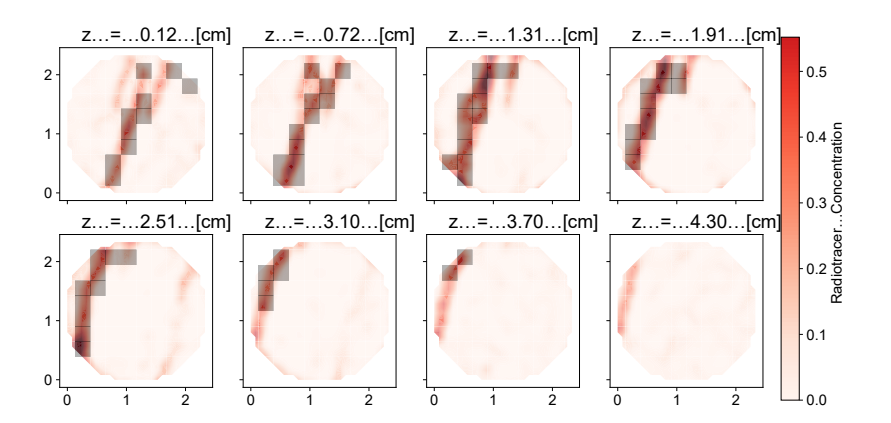


Figure 4: Two-dimensional slices through the core in the PET scan after acid exposure after 143 minutes of tracer injection. The slices are at increasing distances from the inlet (z=0). X and Y axes are length scales in centimeters. The red color scale gives radiotracer concentration and the shaded grey boxes highlight the coarsened thresholded voxels used for fitting the analytical transport model.

The line colors in Figures 5 and 6 are based on voxel distance from the inlet of the core. In all voxels, the matrix tortuosity, fracture dispersivity, and fracture advection velocity were determined by fitting the analytical model to the breakthrough curves in the voxels containing fractures. It is clear from these figures that the analytical model was able to capture the trends in the measured concentrations despite the simplifying assumptions of the analytical model.

Statistical distributions of the fit parameters from the tracer tests before and after low-pH brine injection are illustrated in the histograms in Figure 7. The histogram of matrix tortuosity values indicates that there is a slight shift toward higher matrix tortuosity and therefore higher effective matrix diffusion following low-pH brine injection—with the mean matrix tortuosity increasing from 0.038 to 0.040. The histogram of fracture dispersivity indicates that dispersivity is slightly higher following acid exposure and the fracture advection velocity is slightly lower and has a more uniformly distributed following low-pH brine injection.

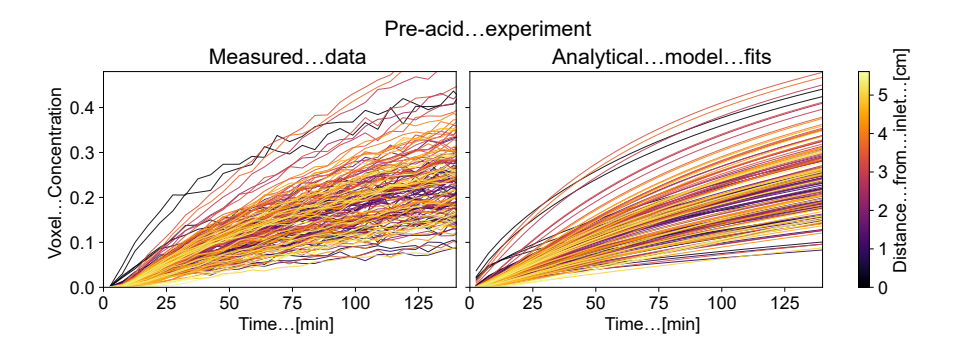


Figure 5: (left) Breakthrough curves for every voxel in the fracture determined from the PET scan prior to low-pH brine injection, as determined from the Frangi filter segmentation method described in Section 2.5. (right) Corresponding analytical fits to each voxel breakthrough curve. The colors in the analytical fit correspond to the same color of each voxel of measured data. The line color corresponds to the approximate distance from the inlet of the core in centimeters as described by the colorbar.

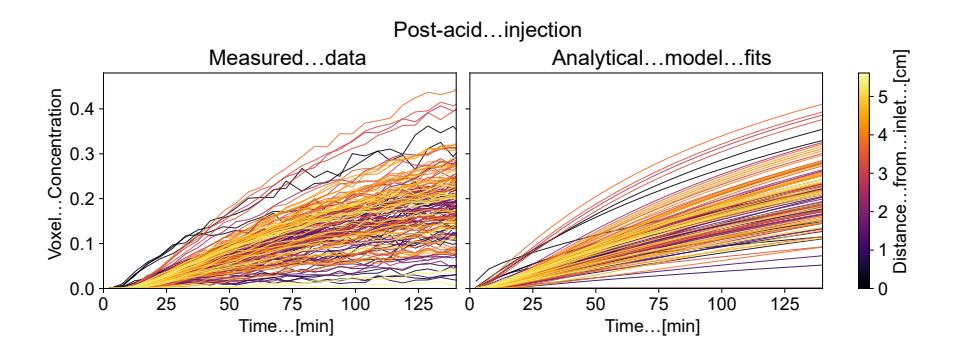


Figure 6: (left) Breakthrough curves for every voxel measured in the fracture using the PET scan taken after low-pH brine injection. (right) Corresponding analytical fits to each voxel breakthrough curve. The colors in the analytical fit correspond to the same color of each voxel of measured data. The line color corresponds to the approximate distance from the inlet of the core in centimeters as indicated by the colorbar.

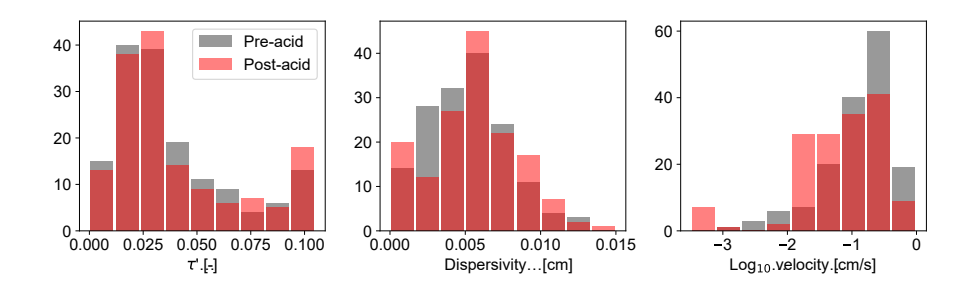


Figure 7: Histogram of fit matrix tortuosity values (left) describing matrix diffusion, fracture dispersivity (center), and fracture advection velocity (right) before and after low-pH brine injection—indicated by grey and red shading, respectively.

## 3.3. One-dimensional reactive transport simulations of acidified fluid injection

The results of the 1D reactive transport simulation described in Section 2.7 are illustrated in Figure 8. The transport of reactive species within the matrix is almost entirely driven by diffusion. The results illustrate increasing porosity at the fracture-matrix interface caused by the rapid dissolution of dolomite as a function of injection time. Due to the reactivity of carbonate minerals, the dissolution front only progresses away from the fracture after all dolomite minerals have been dissolved. While these carbonates are still present, the acid is neutralized and reactivity is arrested. If reactive fluid injection was conducted for a longer period of time or with lower pH-brine, dissolution of additional minerals such as K-feldpsar, albite, smectite, and pyrite would lead to further porosity reduction over longer timescales as illustrated by the small volume changes of these minerals in the plots in Appendix C. As noted in Section 2.1, pyrite oxidation is assumed to be minimal because the sample was vacuumed and purged with CO<sub>2</sub> prior to saturating with brine that was purged with nitrogen gas prior to injection.

## 372 4. Discussion

The workflow of PET imaging, fracture-containing-voxel segmentation, and analytical model fitting demonstrates one of the first direct approaches for

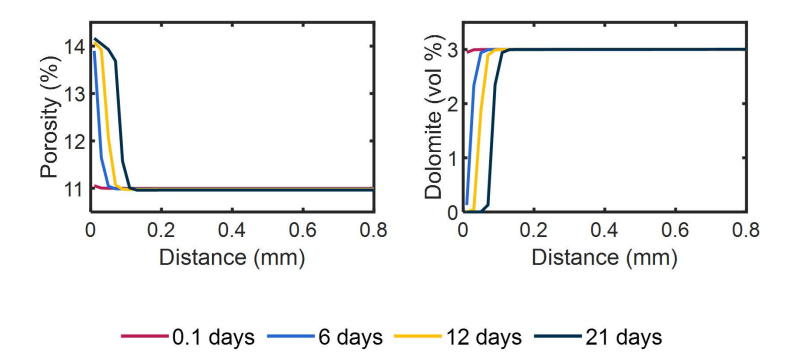


Figure 8: (Left) Model results of predicted porosity increase as a function of distance perpendicular to the fracture-matrix interface over a period of 21 days. (Right) Model output describing the reduction in dolomite volume in the matrix at increasing distance from the fracture-matrix interface due to dissolution.

millimeter-scale quantification of solute transport throughout a centimeter-scale 375 shale core sample. This provides new insights into the distribution of parameters 376 associated with transport through complex fracture geometry and diffusion into 377 a spatially heterogeneous matrix. While a number of analytical solutions exist 378 for describing the extent of fracture-matrix transport, the solution of Tang et al 379 [24] is most applicable to the estimation of transport in the naturally fractured 380 shale sample where advection in the matrix can be assumed to be negligible 38: and the solute concentration in the fracture can not be assumed to be constant. Other analytical models could be substituted into this type of workflow 383 based on the extent of matrix advection or differences in experimental boundary 384 conditions or initial conditions. 385

The matrix tortuosity results in Figure 7 further justify the application of this analytical model which assumes that the vast majority of the tracer stays within the fracture-containing voxels over the time period of the model fit (144 minutes). Integrating the solution to the diffusion equation with respect to distance and using upper 80th percentile matrix tortuosity of  $\tau' = 0.058$  indicates that 90.6% of the tracer would diffuse a distance less than half of the distance of the voxel size of 0.23 cm. At the median matrix tortuosity post-acid

387

388

389

390

392

of  $\tau'=0.029,~97.5\%$  of the tracer would diffuse a distance less than the voxel half-length.

The matrix tortuosity values calculated with this method also agree well with values from literature measured in similar rocks and at similar spatial scales. Published matrix tortuosity values at similar spatial scales are the most directly 397 comparable as reviews of previous studies have observed scale dependence in 398 field measurements [67], similar to the scale dependence observed for dispersion [68]. At the laboratory scale, the typical approach for the quantification of 400 diffusion relies on bulk measurements of gas diffusion into or through samples 401 and corresponding analytical model fits [69, 70, 64, 71]. The methods in this 402 study are analogous to these approaches with the exception that an analytical 403 model can be applied to every voxel of the image-based data, as opposed to 404 typical bulk sample-average measurements. This image-based method results in hundreds of measurements of matrix tortuosity in a given sample. Measurements 406 of matrix tortuosity reported in previous studies of low permeability samples 407 include low permeability limestones 0.031-0.051 [62], a clay-rich marl 0.005 [70], 408 and other low permeability samples where lithology was not specified 0.0082 409 [64], 0.004 - 0.01 [72]. In an extensive study of light hydrocarbon diffusion 410 in sedimentary rocks, Krooss and Leythaeuser [69, 73] measured bulk matrix 411 tortuosity values ranging from 0.002 to 0.077 with a mean of 0.036 in ten different 412 siltstone and shale samples. Thus, the image-based approach for local diffusion 413 and matrix tortuosity quantification in this study agrees well with previous results in rocks of similar lithology. 415

The local advection rates calculated from the analytical fitting range from 0.001 cm/s to 0.6 cm/s in the pre-acid experiments and from 0.0007 cm/s to 0.5 cm/s in the post-acid experiments. The mean pre-acid advection velocity is 0.2 cm/s while the mean post-acid advection velocity was 0.14 cm/s. These mean velocities would suggest a mean fracture aperture of around four micrometers based on an injection rate of 0.013 mL/min and assuming a single fracture that is 2.54 cm wide—the same width as the core. These values are reasonable given the micro-Darcy permeability of the shale core, the presence of channelized

416

417

418

419

420

421

422

flow within fractures that is apparent in the PET images, and the complexity of flow and transport between multiple fractures along the axis of the core. 425 Note however that the calculated dispersivity and advection velocity values are strongly dependent on a relatively small number of early-time concentration 427 measurements and analytical model assumptions about the linear distance of 428 the voxel from the inlet of the core. Therefore these parameters are more prone 429 to model fitting errors than the matrix tortuosity values that are constrained 430 by a larger number of long-time concentration measurements reflecting fracture-431 matrix diffusion. 432

The reactive transport simulations independently support the experimen-433 tal image-based observations, suggesting that acid exposure could enhance the 434 porosity of the matrix near the fracture-matrix interface—depending on the lo-435 cal mineralogical carbonate content. Specifically, the dissolution of dolomite in the matrix shown in the right plot of Figure 8 corresponds to a subtle increase in 437 porosity shown in the left plot of Figure 8 at the fracture-matrix interface. This 438 dissolution is consistent with the slight increase in the matrix tortuosity follow-439 ing acid exposure. However as shown in the left plot in Figure 7, this increase 440 in tortuosity is not widespread and seems to be restricted to small subregions 441 of the fractures. 442

In addition to enhanced connectivity, previous studies have shown that 443 extended matrix exposure to acidic pH conditions results in shale softening 444 [74, 75, 6]. Low pH conditions drive reactions in mineralogically heterogeneous shales that have been observed to increase surface roughness, drive fines mi-446 gration, and induce clay swelling [6]. Our observations of an approximately 447 linear permeability reduction from 15  $\mu$ D to 7  $\mu$ D over the course of the 21 day 448 pH 4.0 brine injection experiment, combined with the more uniform advection 449 velocities after low-pH brine injection shown in Figure 7, suggest reduced flow 450 channelization and softening at the fracture-matrix interface. It is also possible 451 that there was some mechanical deformation to fracture asperities due to pres-452 surizing and depressurizing the confining pressure on the core during transport 453 between imaging facilities.

## 55 5. Conclusion

In this study, slug tracer experiments were performed in a naturally fractured 456 Wolfcamp shale core and imaged with positron emission tomography before 457 and after 21 days of injection of a low pH brine. Imaging results were used 458 to quantify fracture-matrix transport by fitting a solution to the advectiondispersion equation [24]. This image-based transport quantification enabled the 460 local voxel-level determination of matrix tortuosity, fracture dispersivity, and 461 local advection velocity in over 150 unique locations throughout the core sample. 462 Distributions of local tortuosity and fracture advection velocity distributions, 463 combined with 1D reactive transport simulations, indicate subtle changes in diffusivity and likely shale softening at the fracture-matrix interface. This shale 465 softening and reduced channelization led to lower permeability and reduced 466 fracture channelization following exposure to low pH conditions. 467

The experimental imaging workflow and transport parameterization demon-468 strated in this study provides a new approach for understanding the spatial and temporal evolution of flow and transport behavior in naturally fractured 470 core samples. These multiscale observations and models improve mechanistic 471 understanding and scale translation of flow and reactive transport processes in 472 shale formations in response to transient changes in pore fluid chemistry. This 473 understanding is key for the management of groundwater resources, storage se-474 curity of geologically sequestered CO<sub>2</sub>, resource recovery following hydraulic 475 fracturing, and long-term nuclear waste repository design. 476

## Acknowledgements

Datasets and analytical modeling and analysis codes are available at the
Stanford Data Repository [76]. The experimental system used for column and
imaging experiments was supported by the National Science Foundation under
Grant No. 2002412. Any opinions, findings, and conclusions or recommendations expressed in this material are those of the authors and do not necessarily
reflect the views of the National Science Foundation. This work was supported

as part of the Center for Mechanistic Control of Unconventional Formations (CMC-UF), an Energy Frontier Research Center funded by the U.S. Department of Energy, Office of Science under DOE (BES) Award DE-SC0019165. Further support for this research was provided by the Office of the Vice Chancellor for Research and Graduate Education at the University of Wisconsin-Madison with funding from the Wisconsin Alumni Research Foundation.

## 490 Appendix A. Shale sample mineral composition

Table A.3 summarizes the mineral composition in weight percentage of the
Wolfcamp sample used in the experiments.

Table A.3: Mineral composition of the Wolfcamp sample.

Mineral	Quartz	K-Feldspar	Plagioclase	Calcite	Dolomite	Pyrite	Illite	Mixed Il- lite/Smecti	Organic te Matter
wt%	62.1	0.8	4.8	0.2	3.7	2.6	19.4	6.4	2.7

## 493 Appendix B. Concatenating multiple PET scans

501

502

503

Figure B.9 illustrates the PET scan concatenation and decay correction back to the beginning of the first scan. Our recent work verified that radioactivity is conserved across multiple scans after decay correction [48]. The uncorrected (dashed line) in Figure B.9 also illustrates how the signal from the radiotracer decreases through time due to the radioactive decay of the 110-minute half-life 18F radioisotope.

## Appendix C. Reactive transport results for non carbonate species

Table C.4 and C.5 show the aqueous reactions and mineral kinetic reactions respectively. Aqueous kinetic reactions respect a rate-dependent transition state theory (TST) rate law as shown in Equation C.1 [77] where  $\prod (a_i)^n$  indicates the product of rate dependency on all aqueous species,  $K_{eq}$  refers to equilibrium

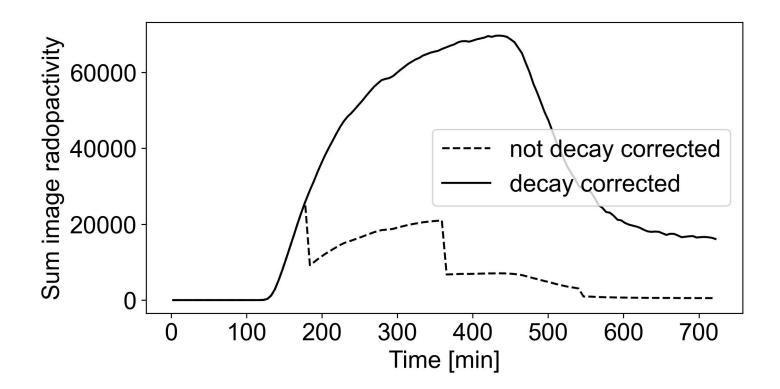


Figure B.9: Total activity in core as a function of time in PET scan prior to acidified brine injection.

constant, k is the reaction rate constant in mol(kg water)<sup>-1</sup>yr<sup>-1</sup>, and IAP is the ion activity product.

$$R = k \prod (a_i)^n \left[1 - \frac{\text{IAP}}{K_{eq}}\right] \tag{C.1}$$

Mineral dissolution and precipitation also respect a TST rate law as shown in Equation C.2 [77] where  $\prod$   $(a_i)^n$  shows rate dependency on species a,  $K_{sp}$  refers to solubility product of the mineral, k is the rate constant in mol·m<sup>-2</sup>s<sup>-1</sup>,  $A_m$  is mineral surface area in m<sup>2</sup>s<sup>-1</sup>, and IAP is the ion activity product. Temperature dependence of the rate constants are accounted for by the CrunchFlow numerical simulator using the Arrhenius equation.  $A_m$  is set to one for pre-existing minerals and set to 0.1 for secondary minerals that may precipitate such as gypsum, halite, Fe(OH)<sub>3</sub>, and amorphous SiO<sub>2</sub>.

$$R = A_m k \prod (a_i)^n \left[1 - \frac{\text{IAP}}{K_{eq}}\right]$$
 (C.2)

Additional observations from the reactive transport model suggest volume reduction of K-feldspar, albite, pyrite, and smectite with time due to dissolution that occurs at a significantly lower rate than carbonates (Figure C.10). These plots show that the precipitation of pyrite is followed immediately after dissolution.

515

516

517

518

Table C.4: Instantaneous aqueous speciation reactions considered in the reactive transport model. The equilibrium constants are reported for  $40^{\circ}$ C and derived from Li et al [78].

Equilibrium Reactions [78]	$\log_{10}(K_{eq})$ [78]
$Fe^{3+} + 0.5H_2O \leftrightarrow Fe^{2+} + H^+ + 0.25O_2(aq)$	-7.66
$AlOH^{2+} + H^+ \leftrightarrow Al^{3+} + H_2O$	4.53
$Al(OH)_2^+ + 2H^+ \leftrightarrow Al^{3+} 2H_2O$	9.76
$Al(SO)_4^+ \leftrightarrow SO_4^{2-} + Al^{3+}$	-3.01
$MgCl^+ \leftrightarrow Cl^- + Mg^{2+}$	0.12
$\rm H_2S(aq)\leftrightarrow H^+ + HS^-$	-6.81
$\mathrm{H_2SO_4(aq)} \leftrightarrow \mathrm{2H^+} + \mathrm{SO_4^{2-}}$	1.02
$\mathrm{HSO}_4^- \leftrightarrow \mathrm{H}^+ + \mathrm{SO}_4^{2-}$	-2.14
$CaCl^+ \leftrightarrow Ca^{2+} + Cl^-$	0.67
$CaCl_2(aq) \leftrightarrow Ca^{2+} + 2Cl^{-}$	0.67
$CaOH^+ + H^+ \leftrightarrow Ca^{2+} + H_2O$	12.9
$CaSO_4(aq) \leftrightarrow Ca^{2+} + SO_4^{2-}$	-2.16
$HCl(aq) \leftrightarrow H^+ + Cl^-$	-0.69
$\mathrm{H^+} + \mathrm{OH^-} \leftrightarrow \mathrm{H_2O}$	13.54
$CO_2(aq) + H_2O \leftrightarrow H^+ + HCO_3^-$	-6.28
$\mathrm{CO}_3^{2-} + \mathrm{H}^+ \leftrightarrow \mathrm{HCO}_3^-$	10.22

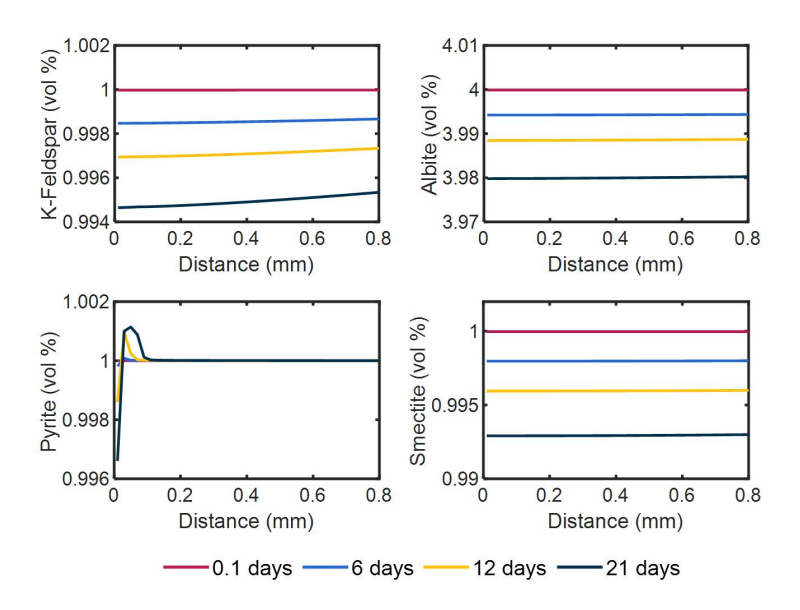


Figure C.10: Volume reductions of K-feldspar (upper left), albite (upper right), pyrite (lower left), and smectite (lower right) indicate slow dissolution of these minerals at the fracture-matrix interface.

Table C.5: Mineral kinetic reactions and their model parameters.  $\Pi(a_i)^n$  shows rate dependency on species a,  $\log_{10}(K_{sp})$  is solubility product of minerals at  $40^{\circ}$ C and  $\log_{10}(k)$  is the rate constant in  $\text{mol·m}^{-2}\text{s}^{-1}$  shown for  $25^{\circ}$ C.

Minerals	Reactions [78]	$\prod (a_i)^n [78]$	$\log_{10}(\mathbf{K}_{sp}) [78]$	$\log_{10}(k)$
Quartz	Quartz $\leftrightarrow SiO_2(aq)$	None	-3.74	-15[78]
K-Feldspar	K-Feldspar + $4H^+ \leftrightarrow Al^{3+}$	None	-0.53	-11.5[79]
	$+ K^{+} + 2H_{2}O + 3SiO_{2}(aq)$			
Albite	Albite + $4H^+ \leftrightarrow Al^{3+} +$	None	2.27	-11.5[80, 81]
	$Na^+ + 2H_2O + 3SiO_2(aq)$			
Calcite	Calcite + $H^+ \leftrightarrow Ca^{2+} +$	$(H^+)^{1.0}$	1.63	-3.5[78]
	HCO <sub>3</sub>			
Dolomite	Dolomite $+ 2H^+ \leftrightarrow Ca^{2+} +$	$({\rm H}^+)^{0.5}$ , None	2.0	-7.7[78]
	$\mathrm{Mg}^{2+} + 2\mathrm{HCO}_{3}^{-}$			
Pyrite	Pyrite + $H_2O \leftrightarrow Fe^{2+}$ +	None	-23.75	-7.5[80, 82]
	$1.75 \text{HS}^- + 0.25 \text{SO}_4^{2-} +$			
	0.25H <sup>+</sup>			
Illite	Illite + $8H^+ \leftrightarrow 0.25Mg^{2+}$	None	7.51	-11[78]
	$+ 0.6K^{+} + 2.3Al^{3+}$			
	$3.5 \mathrm{SiO}_2(\mathrm{aq}) + 5 \mathrm{H}_2 \mathrm{O}$			
Smectite	Smectite $+$ $7H^+ \leftrightarrow$	None	8.53	-11[80, 83]
	$0.02Ca^{2+} + 0.15Na^{+} +$			
	$0.16 \text{Fe}^{3+} + 0.2 \text{K}^{+} +$			
	$0.29 \text{Fe}^{3+} + 0.9 \text{Mg}^{2+} +$			
	$1.25 \text{Al}^{3+} + 3.75 \text{SiO}_2(\text{aq})$			
Gypsum	$Gypsum \leftrightarrow Ca^{2+} + SO_4^{2-}$	None	-4.51	-30[78]
Halite	$Halite \leftrightarrow Na^+ + Cl^-$	None	1 61	-0.21[80, 84]
$Fe(OH)_3$	$Fe(OH)_3 + 3H^+ \leftrightarrow Fe^{3+} +$	$(H^+)^{1.0}$	-5.30	-8.5[78]
	3H <sub>2</sub> O			
$SiO_2(am)$	$SiO_2(am) \leftrightarrow SiO_2(aq)$	None	-2.56	-8[78]

#### References

- [1] A. Vengosh, R. B. Jackson, N. Warner, T. H. Darrah, A. Kondash, A. 521 critical review of the risks to water resources from unconventional shale gas 522 development and hydraulic fracturing in the United States, Environmental 523 Science and Technology 48 (15) (2014) 8334–8348. doi:10.1021/es405118y. 524
- [2] M. A. Ferno, L. P. Hauge, A. Uno Rognmo, J. Gauteplass, A. Graue, M. A. 525 Fernø, L. P. Hauge, A. Uno Rognmo, J. Gauteplass, A. Graue, Flow visual-526 ization of CO2 in tight shale formations at reservoir conditions, Geophysical 527 Research Letters 42 (18) (2015) 7414-7419. doi:10.1002/2015GL065100. 528
- URL http://doi.wiley.com/10.1002/2015GL065100
- [3] C. Zahasky, S. Benson, Evaluation of hydraulic controls for leakage inter-530 vention in carbon storage reservoirs, International Journal of Greenhouse 531 Gas Control 47 (2016) 86–100. doi:10.1016/j.ijggc.2016.01.035. 532
- [4] Q. C. Wenning, C. Madonna, T. Kurotori, C. Petrini, J. Hwang, A. Zap-533 pone, S. Wiemer, D. Giardini, R. Pini, Chemo-Mechanical Coupling in 534 Fractured Shale With Water and Hydrocarbon Flow, Geophysical Research 535 Letters 48 (5) (2021) 0–12. doi:10.1029/2020GL091357. 536
- [5] Q. Li, A. D. Jew, A. Kohli, K. Maher, G. E. Brown, J. R. Bargar, Thick-537 nesses of Chemically Altered Zones in Shale Matrices Resulting from Inter-538 actions with Hydraulic Fracturing Fluid, Energy and Fuels 33 (8) (2019) 6878-6889. doi:10.1021/acs.energyfuels.8b04527. 540
- [6] H. J. Khan, E. Spielman-Sun, A. D. Jew, J. Bargar, A. Kovscek, J. L. 541 Druhan, A Critical Review of the Physicochemical Impacts of Water Chem-542 istry on Shale in Hydraulic Fracturing Systems, Environmental Science and Technology 55 (3) (2021) 1377–1394. doi:10.1021/acs.est.0c04901.
- [7] B. F. Esteves, E. Spielman-Sun, Q. Li, A. D. Jew, J. R. Bargar, J. L. 545 Druhan, Geochemical modeling of celestite (srso4) precipitation and reac-546

- tive transport in shales, Environmental Science & Technology 56 (7) (2022) 4336-4344.
- [8] D. Sassani, C. Stone, F. Hansen, E. Hardin, T. Dewers, M. Martinez,
- R. Rechard, S. Sobolik, G. Freeze, R. Cygan, K. Gaither, J. Holland,
- P. Brady, Shale disposal of U.S. high-level radioactive waste., Tech. Rep.
- May, Sandia National Laboratories (SNL), Albuquerque, NM, and Liver-
- more, CA (United States) (may 2010). doi:10.2172/992338.
- URL https://www.osti.gov/servlets/purl/992338/
- 555 [9] L. F. Orellana, C. Giorgetti, M. Violay, Contrasting me-
- chanical and hydraulic properties of wet and dry fault
- zones in a proposed shale-hosted nuclear waste reposi-
- tory, Geophysical Research Letters 46 (3) (2019) 1357–1366.
- arXiv:https://agupubs.onlinelibrary.wiley.com/doi/pdf/10.1029/2018GL080384,
- doi:https://doi.org/10.1029/2018GL080384.
- URL https://agupubs.onlinelibrary.wiley.com/doi/abs/10.1029/2018GL080384
- [10] J. Warren, P. Root, The Behavior of Naturally Fractured Reservoirs, Soci-
- ety of Petroleum Engineers Journal 3 (03) (1963) 245–255. doi:10.2118/426-
- 564 pa.
- 565 [11] K. Pruess, T. N. Narasimhan, A Practical Method for
- Modeling Fluid and Heat Flow in Fractured Porous Me-
- dia, Society of Petroleum Engineers Journal 25 (01)
- 568 (1985) 14–26. arXiv:https://onepetro.org/spejournal/article-
- pdf/25/01/14/2647668/spe-10509-pa.pdf, doi:10.2118/10509-PA.
- URL https://doi.org/10.2118/10509-PA
- [12] B. Berkowitz, J. Bear, C. Braester, Continuum models for contaminant
- transport in fractured porous formations, Water Resources Research 24 (8)
- 573 (1988) 1225–1236. doi:10.1029/WR024i008p01225.
- 574 [13] H. H. Gerke, M. van Genuchten, Dual porosity model for simulating the

- prefrential movement of water and solutes in structured porous media, Wa-575 ter Resources Research 29 (2) (1993) 305-319. 576
- [14] B. W. Arnold, H. Zhang, A. M. Parsons, Effective-porosity and dual-577 porosity approaches to solute transport in the saturated zone at yucca 578 mountain: Implications for repository performance assessment, Geophysi-579 cal Monograph Series 122 (2000) 313–322. doi:10.1029/GM122p0313. 580
- [15] J. D. Hyman, S. Karra, N. Makedonska, C. W. Gable, S. L. Painter, H. S. 583 Viswanathan, DfnWorks: A discrete fracture network framework for mod-582 eling subsurface flow and transport, Computers and Geosciences 84 (2015) 583 10-19. doi:10.1016/j.cageo.2015.08.001. 584 URL http://dx.doi.org/10.1016/j.cageo.2015.08.001
- [16] C. R. Romano, R. T. Williams, Evolution of Fault-Zone Hydromechanical Properties in Response to Different Cementation Processes, Lithosphere 587 2022 (1) (2022). doi:10.2113/2022/1069843. 588
- [17] M. B. Cardenas, D. T. Slottke, R. A. Ketcham, J. M. S. Jr, Navier-589 Stokes flow and transport simulations using real fractures shows heavy tailing due to eddies, Geophysical Research Letters 34 (July) (2007) 1–6. 591 doi:10.1029/2007GL030545. 592
- [18] S. Yoon, P. K. Kang, Roughness, inertia, and diffusion effects on anoma-593 lous transport in rough channel flows, Physical Review Fluids 6 (1) (2021) 594 14502. doi:10.1103/PhysRevFluids.6.014502. 595 URL https://doi.org/10.1103/PhysRevFluids.6.014502
- [19] C. Soulaine, P. Creux, H. A. Tchelepi, Micro-continuum Framework for 597 Pore-Scale Multiphase Fluid Transport in Shale Formations, Transport in
- Porous Media 127 (1) (2019) 85–112. doi:10.1007/s11242-018-1181-4. 599
- URL https://doi.org/10.1007/s11242-018-1181-4 600

596

Q. Zhang, H. Deng, Y. Dong, S. Molins, X. Li, C. Steefel, Investigation 601 of Coupled Processes in Fractures and the Bordering Matrix via a Micro-602

- Continuum Reactive Transport Model, Water Resources Research 58 (2) (2022) 1–18. doi:10.1029/2021WR030578.
- [21] I. Neretnieks, Diffusion in the rock matrix: An important factor in radionuclide retardation?, Journal of Geophysical Research 85 (B8) (1980) 4379.

  doi:10.1029/JB085iB08p04379.
- [22] B. Berkowitz, J. Zhou, Reactive solute transport in a single fracture, Water
   Resources Research 32 (4) (1996) 901–913. doi:10.1029/95WR03615.
- [23] M. T. V. Genuchten, W. J. Alves, Analytical Solutions of the 1D
   Convective-Dispersive Solute Transport Equation, Tech. Rep. 1661, U.S.
   Department of Agriculture, Beltsville, MD (1982).
- [24] D. H. Tang, E. O. Frind, E. A. Sudicky, Contaminant transport in fractured
   porous media: Analytical solution for a single fracture, Water Resources
   Research 17 (3) (1981) 555–564. doi:10.1029/WR017i003p00555.
   URL http://doi.wiley.com/10.1029/WR017i003p00555
- [25] D. Roubinet, J. R. De Dreuzy, D. M. Tartakovsky, Semi-analytical solutions for solute transport and exchange in fractured porous media, Water Resources Research 48 (1) (2012) 1–10. doi:10.1029/2011WR011168.
- [26] G. Dávila, L. Luquot, J. M. Soler, J. Cama, 2D reactive transport modeling of the interaction between a marl and a CO2-rich sulfate solution under supercritical CO2 conditions, International Journal of Greenhouse Gas Control 54 (2016) 145–159. doi:10.1016/j.ijggc.2016.08.033.

  URL http://dx.doi.org/10.1016/j.ijggc.2016.08.033
- [27] H. Deng, M. Voltolini, S. Molins, C. Steefel, D. DePaolo, J. Ajo-Franklin,
   L. Yang, Alteration and Erosion of Rock Matrix Bordering a Carbonate Rich Shale Fracture, Environmental Science and Technology 51 (15) (2017)
   8861–8868. doi:10.1021/acs.est.7b02063.
- [28] A. D. Jew, J. L. Druhan, M. Ihme, A. R. Kovscek, I. Battiato, J. P.
   Kaszuba, J. R. Bargar, G. E. Brown Jr, Chemical and reactive transport

- processes associated with hydraulic fracturing of unconventional oil/gas shales, Chemical reviews 122 (9) (2022) 9198–9263.
- [29] Y. Zhang, P. Mostaghimi, A. Fogden, A. Sheppard, A. Arena, J. Middleton,
   R. T. Armstrong, Time-Lapsed Visualization and Characterization of Shale
   Diffusion Properties Using 4D X-ray Microcomputed Tomography, Energy
   and Fuels 32 (3) (2018) 2889–2900. doi:10.1021/acs.energyfuels.7b03191.
- [30] C. I. Steefel, K. T. MacQuarrie, Approaches to modeling of reactive transport in porous media, Reactive transport in porous media (2018) 83–130.
- [31] J. M. Galíndez, J. Molinero, Assessment of the long-term stability of cementitious barriers of radioactive waste repositories by using digital-imagebased microstructure generation and reactive transport modelling, Cement and Concrete Research 40 (8) (2010) 1278–1289.
- [32] M. Xie, K. U. Mayer, F. Claret, P. Alt-Epping, D. Jacques, C. Steefel, C. Chiaberge, J. Simunek, Implementation and evaluation of permeabilityporosity and tortuosity-porosity relationships linked to mineral dissolutionprecipitation, Computational Geosciences 19 (3) (2015) 655–671.
- [33] K. T. MacQuarrie, K. U. Mayer, Reactive transport modeling in fractured
   rock: A state-of-the-science review, Earth Science Reviews 72 (3-4) (2005)
   189–227.
- [34] C. I. Steefel, D. J. DePaolo, P. C. Lichtner, Earth and planetary science
   letters, Reactive transport in porous media (3-4) (2005) 539–558.
- [35] C. Steefel, C. Appelo, B. Arora, D. Jacques, T. Kalbacher, O. Kolditz,
   V. Lagneau, P. Lichtner, K. U. Mayer, J. Meeussen, et al., Reactive trans port codes for subsurface environmental simulation, Computational Geosciences 19 (3) (2015) 445–478.
- [36] J. Druhan, C. Tournassat, M. S. of Mineralogical Society of America, Re active transport in natural and engineered systems, Vol. 85, Mineralogical
   Society of America, 2019.

- [37] H. J. Khan, C. M. Ross, J. L. Druhan, Impact of concurrent solubilization and fines migration on fracture aperture growth in shales during
   acidized brine injection, Energy & Fuels 36 (11) (2022) 5681–5694.
   doi:https://doi.org/10.1021/acs.energyfuels.2c00611.
   URL https://pubs.acs.org/doi/full/10.1021/acs.energyfuels.2c00611
- [38] M. H. Bradbury, A. Green, Measurement of important parameters determining aqueous phase diffusion rates through crystalline rock matrices, Journal of Hydrology 82 (1-2) (1985) 39–55. doi:10.1016/0022-1694(85)90045-9.
- [39] K. Skagius, I. Neretnieks, Diffusivity Measurements and Electrical Resistivity Measurements in Rock Samples Under Mechanical Stress, Water Resources Research 22 (4) (1986) 570–580. doi:10.1029/WR022i004p00570.

  URL http://doi.wiley.com/10.1029/WR022i004p00570
- [40] A. S. Grader, M. Balzarini, F. Radaelli, G. Capasso, A. Pellegrino,
   Fracture-matrix flow: Quantification and visualization using X-Ray
   computerized tomography, 2000, pp. 157–168. doi:10.1029/GM122p0157.
   URL http://www.agu.org/books/gm/v122/GM122p0157/GM122p0157.shtml
- [41] S. Akin, A. Kovscek, Computed Tomography in Petroleum Engineering
   Research, Applications of X-ray Computed Tomography in the Geosciences
   215 (2003) 23–38.
- [42] A. Polak, D. Elsworth, H. Yasuhara, A. S. Grader, P. M. Halleck,
  Permeability reduction of a natural fracture under net dissolution by
  hydrothermal fluids, Geophysical Research Letters 30 (20) (2003) 1–4.
  doi:10.1029/2003GL017575.
- [43] B. R. Ellis, J. P. Fitts, G. S. Bromhal, D. L. McIntyre, R. Tappero, C. A.
   Peters, Dissolution-driven permeability reduction of a fractured carbon ate caprock, Environmental Engineering Science 30 (4) (2013) 187–193.
   doi:10.1089/ees.2012.0337.

- [44] H. Deng, J. P. Fitts, D. Crandall, D. McIntyre, C. A. Peters, Alterations of Fractures in Carbonate Rocks by CO2-Acidified Brines,
   Environmental Science and Technology 49 (16) (2015) 10226–10234.
   doi:10.1021/acs.est.5b01980.
- [45] C. Zahasky, T. Kurotori, R. Pini, S. M. Benson, Positron emission tomography in water resources and subsurface energy resources engineering research, Advances in Water Resources 127 (March) (2019) 39–52.
  doi:10.1016/j.advwatres.2019.03.003.
- URL https://doi.org/10.1016/j.advwatres.2019.03.003
- [46] C. Zahasky, D. Thomas, J. Matter, K. Maher, S. M. Benson, Multimodal imaging and stochastic percolation simulation for improved quantification of effective porosity and surface area in vesicular basalt, Advances in Water Resources 121 (June) (2018) 235–244. doi:10.1016/j.advwatres.2018.08.009.
   URL https://doi.org/10.1016/j.advwatres.2018.08.009
- [47] S. Li, L. Liu, P. Chai, X. Li, J. He, Z. Zhang, Journal of Petroleum Science and Engineering Imaging hydraulic fractures of shale cores using combined positron emission tomography and computed tomography (PETCT) imaging technique, Journal of Petroleum Science and Engineering
  182 (May) (2019) 106283. doi:10.1016/j.petrol.2019.106283.

  URL https://doi.org/10.1016/j.petrol.2019.106283
- To [48] T. Kurotori, C. Zahasky, M. Gran, A. R. Kovscek, S. M. Benson, Comparative analysis of imaging and measurements of micrometer-scale fracture aperture fields within a heterogeneous rock using PET and X-ray CT, Transport in Porous Media 147 (2023) 519–539. doi:https://doi.org/10.1007/s11242-023-01922-8.
- [49] C. Zahasky, S. M. Benson, Micro-Positron Emission Tomography for
   Measuring Sub-core Scale Single and Multiphase Transport Parameters in Porous Media, Advances in Water Resources 115 (2018) 1–16.

- doi:10.1016/j.advwatres.2018.03.002.
  URL http://linkinghub.elsevier.com/retrieve/pii/S030917081731182X
- 717 [50] C. R. Romano, C. Zahasky, C. Garing, J. M. Minto, S. M. Benson, Z. K.
  718 Shipton, R. J. Lunn, Sub-core scale fluid flow behavior in a sandstone
  719 with cataclastic deformation bands, Water Resources Research (2020) 1—
  720 16doi:10.1029/2019wr026715.
- [51] C. Zahasky, S. M. Benson, Preferential Solute Transport in Low Permeability Zones During Spontaneous Imbibition in Heterogeneous Porous Media,
   Water Resources Research 58 (1) (2022). doi:10.1029/2020wr029460.
- [52] T. Kurotori, C. Zahasky, S. Hosseinzadeh Hejazi, S. Shah, S. Benson, R. Pini, Measuring, imaging and modelling solute transport in a microporous limestone, Chemical Engineering Science 196 (2019).
   doi:10.1016/j.ces.2018.11.001.
- [53] T. Kurotori, M. P. Murugesu, C. Zahasky, B. Vega, J. L. Druhan, S. M.
   Benson, A. R. Kovscek, Mixed imbibition controls the advance of wetting
   fluid in multiscale geological media, Advances in Water Resources 175
   (2023) 104429. doi:https://doi.org/10.1016/j.advwatres.2023.104429.
   URL https://www.sciencedirect.com/science/article/pii/S0309170823000647
- 733 [54] R. Pini, S. C. Krevor, S. M. Benson, Capillary pressure and het-734 erogeneity for the CO2/water system in sandstone rocks at reser-735 voir conditions, Advances in Water Resources 38 (2012) 48–59. 736 doi:10.1016/j.advwatres.2011.12.007. 737 URL http://linkinghub.elsevier.com/retrieve/pii/S0309170811002363
- [55] H. Aljamaan, C. M. Ross, A. R. Kovscek, Multiscale Imaging of Gas Storage
   in Shales, SPE Journal 22 (06) (2017) 1760–1777. doi:10.2118/185054-PA.
   URL http://www.onepetro.org/doi/10.2118/185054-PA
- [56] A. F. Frangi, W. J. Niessen, K. L. Vincken, M. A. Viergever, Multiscale vessel enhancement filtering, in: W. M. Wells, A. Colchester, S. Delp (Eds.),

- Medical Image Computing and Computer-Assisted Intervention MIC-CAI'98, Springer Berlin Heidelberg, Berlin, Heidelberg, 1998, pp. 130–137.
- [57] L. Li, L. Zhu, C. Ma, L. Lin, J. Yao, L. Wang, K. Maslov, R. Zhang,
   W. Chen, J. Shi, L. V. Wang, Single-impulse panoramic photoacoustic
   computed tomography of small-animal whole-body dynamics at high spatiotemporal resolution, Nature Biomedical Engineering 1 (5) (2017) 0071.
   doi:10.1038/s41551-017-0071.
- URL http://www.nature.com/articles/s41551-017-0071
- [58] Y. Liu, L. Peng, S. Huang, X. Wang, Y. Wang, Z. Peng,
   River detection in high-resolution sar data using the frangi fil ter and shearlet features, Remote Sensing Letters 10 (10) (2019)
   949–958. arXiv:https://doi.org/10.1080/2150704X.2019.1635286,
   doi:10.1080/2150704X.2019.1635286.
   URL https://doi.org/10.1080/2150704X.2019.1635286
- 757 [59] R. N. Horne, F. Rodriguez, Dispersion in tracer flow in fractured 758 geothermal systems, Geophysical Research Letters 10 (4) (1983) 289–292. 759 doi:10.1029/GL010i004p00289.
- URL http://doi.wiley.com/10.1029/GL010i004p00289
- [60] I. Ippolito, E. J. Hinch, G. Daccord, J. P. Hulin, Tracer dispersion in 2-D
   fractures with flat and rough walls in a radial flow geometry, Physics of
   Fluids A 5 (8) (1992) 1952–1962. doi:10.1063/1.858822.
- [61] J. Bodin, F. Delay, G. de Marsily, Solute transport in a single fracture with
   negligible matrix permeability: 1. Fundamental mechanisms, Hydrogeology
   Journal 11 (4) (2003) 418–433. doi:10.1007/s10040-003-0268-2.
- [62] L. J. KLINKENBERG, ANALOGY **BETWEEN** DIF-767 **FUSION** AND ELECTRICAL CONDUCTIVITY IN768 ROCKS, GSA62 **POROUS** Bulletin (6)(1951)559-564.

- pdf/62/6/559/3441164/i0016-7606-62-6-559.pdf, doi:10.1130/0016-
- 772 7606(1951)62[559:ABDAEC]2.0.CO;2.
- URL https://doi.org/10.1130/0016-7606(1951)62[559:ABDAEC]2.0.CO;2
- 774 [63] J. van Brakel, P. Heertjes, Analysis of diffusion in macroporous media 775 in terms of a porosity, a tortuosity and a constrictivity factor, Inter-776 national Journal of Heat and Mass Transfer 17 (9) (1974) 1093–1103.
- doi:10.1016/0017-9310(74)90190-2.
- [64] S. Li, Z. Li, Q. Dong, Diffusion coefficients of supercritical CO2 in oil-saturated cores under low permeability reservoir conditions, Journal of CO2
   Utilization 14 (2016) 47–60. doi:10.1016/j.jcou.2016.02.002.
- URL http://dx.doi.org/10.1016/j.jcou.2016.02.002
- [65] R. R. Ratnakar, B. Dindoruk, The Role of Diffusivity in Oil and Gas Industries: Fundamentals, Measurement, and Correlative Techniques, Processes
   10 (6) (2022) 1194. doi:10.3390/pr10061194.
- URL https://www.mdpi.com/2227-9717/10/6/1194
- [66] N. A. Mumallah, Hydrochloric acid diffusion coefficients at acid-fracturing conditions, Journal of Petroleum Science and Engineering 15 (2) (1996)
   361–374. doi:https://doi.org/10.1016/0920-4105(95)00086-0.
- ${\rm URL\ https://www.sciencedirect.com/science/article/pii/0920410595000860}$
- [67] Q. Zhou, H. H. Liu, F. J. Molz, Y. Zhang, G. S. Bodvarsson, Field-scale
   effective matrix diffusion coefficient for fractured rock: Results from liter ature survey, Journal of Contaminant Hydrology 93 (1-4) (2007) 161–187.
   doi:10.1016/j.jconhyd.2007.02.002.
- [68] L. W. Gelhar, C. Welty, K. R. Rehfeldt, A Critical Review of Data on
   Field-Scale Dispersin in Aquifers, Water Resources Research 28 (7) (1992)
   1955–1974. arXiv:arXiv:1011.1669v3, doi:10.1029/92WR00607.

- [69] B. Krooss, R. Schaefer, Experimental measurements of the diffusion
   parameters of light hydrocarbons in water-saturated sedimentary rocks—I.
   A new experimental procedure, Organic Geochemistry 11 (3) (1987)
   193–199. doi:10.1016/0146-6380(87)90022-2.
- URL https://linkinghub.elsevier.com/retrieve/pii/0146638087900222
- [70] V. Rebour, J. Billiotte, M. Deveughele, A. Jambon, C. L. Guen, Molecular diffusion in water-saturated rocks: A new experimental method, Journal of Contaminant Hydrology 28 (1-2) (1997) 71–93. doi:10.1016/S0169-7722(96)00051-4.
- [71] M. G. Rezk, J. Foroozesh, A. Abdulrahman, J. Gholinezhad, CO2Diffusion
   and Dispersion in Porous Media: Review of Advances in Experimental
   Measurements and Mathematical Models, Energy and Fuels 36 (1) (2022)
   133–155. doi:10.1021/acs.energyfuels.1c03552.
- [72] S. Li, Y. Wang, K. Zhang, C. Qiao, Diffusion Behavior of Supercritical CO2
   in Micro- To Nanoconfined Pores, Industrial and Engineering Chemistry
   Research 58 (47) (2019) 21772–21784. doi:10.1021/acs.iecr.9b04750.
- [73] B. M. Krooss, D. Leythaeuser, Experimental measurements of the diffusion parameters of light hydrocarbons in water-saturated sedimentary rocks-II.

  Results and geochemical significance, Organic Geochemistry 12 (2) (1988)

  91–108. doi:10.1016/0146-6380(88)90247-1.
- [74] C. Noiriel. B. Madé, Р. Gouze, Impact of coating develop-817 ment on the hydraulic and transport properties in argillaceous 818 limestone fracture, Water Resources Research 43 (9)(2007).819 arXiv:https://agupubs.onlinelibrary.wiley.com/doi/pdf/10.1029/2006WR005379, 820 doi:https://doi.org/10.1029/2006WR005379. 821 URL https://agupubs.onlinelibrary.wiley.com/doi/abs/10.1029/2006WR005379 822
- [75] J. Du, L. Hu, J. N. Meegoda, G. Zhang, Shale softening: Observations, phenomenological behavior, and mechanisms, Applied Clay Science 161

- (2018) 290-300. doi:https://doi.org/10.1016/j.clay.2018.04.033.

  URL https://www.sciencedirect.com/science/article/pii/S0169131718301935
- [76] C. Zahasky, M. Murugesu, T. Kurotori, C. Sutton, J. Druhan, B. Vega, S. M. Benson, A. Kovscek, Solute transport maps in a naturally fractured shale rock before and after acidified brine injection - 4D imaging dataset and analytical model (2023). doi:https://doi.org/10.25740/pv902jr5822.
- [77] C. I. Steefel, S. Molins, Crunchflow, Software for modeling multicomponent
   reactive flow and transport. User's manual. Lawrence Berkeley National
   Laboratory, Berkeley (2009).
- [78] Q. Li, A. D. Jew, G. E. Brown Jr, J. R. Bargar, K. Maher, Reactive
   transport modeling of shale–fluid interactions after imbibition of fracturing
   fluids, Energy & Fuels 34 (5) (2020) 5511–5523.
- [79] H. C. Helgeson, W. M. Murphy, P. Aagaard, Thermodynamic and kinetic constraints on reaction rates among minerals and aqueous solutions. ii. rate constants, effective surface area, and the hydrolysis of feldspar, Geochimica et Cosmochimica Acta 48 (12) (1984) 2405–2432.
- [80] J. L. Palandri, Y. K. Kharaka, A compilation of rate parameters of water-mineral interaction kinetics for application to geochemical modeling, Tech.
   rep., Geological Survey Menlo Park CA, Menlo Park, CA (United States)
   (2004).
- [81] L. Chou, R. Wollast, Steady-state kinetics and dissolution mechanisms of
   albite, American Journal of Science 285 (10) (1985) 963–993.
- [82] M. A. McKibben, H. L. Barnes, Oxidation of pyrite in low temperature acidic solutions: Rate laws and surface textures, Geochimica et Cosmochimica Acta 50 (7) (1986) 1509–1520.
- [83] A. Bauer, G. Berger, Kaolinite and smectite dissolution rate in high molar
   koh solutions at 35 and 80 c 13 (7) (1998) 905–916.

[84] M. Alkattan, E. H. Oelkers, J.-L. Dandurand, J. Schott, Experimental
 studies of halite dissolution kinetics, 1 the effect of saturation state and the
 presence of trace metals, Chemical Geology 137 (3-4) (1997) 201–219.